Synthesis, structure, electronic and thermal properties of sphalerite CuZn2InS4

ARTICLE

Synthesis, structure, electronic and thermal properties of sphalerite $CuZn_2InS_4$

Oluwagbemiga P. Ojo[a], Wilarachchige D. C. B. Gunatilleke[a], Hagen Poddig[b], Hsin Wang[c], Joshua Martin[d], Dylan J. Kirsch[d,e] and George S. Nolas[a]*

Quaternary chalcogenides continue to be of interest due to the variety of physical properties they possess, as well as their potential for different applications of interest. Investigations on materials with the sphalerite crystal structure have only recently begun. In this study we have synthesized sulfur-based sphalerite quaternary chalcogenides, including off-stoichiometric compositions, and investigated the temperature-dependent electronic, thermal and structural properties of these materials. Insulating to semiconducting transport is observed with stochiometric variation, and analyses of heat capacity and thermal expansion revealed lattice anharmonicity that contributes to the low thermal conductivity these materials possess. We include similar analyses for $CuZn_2InSe_4$ and compare these sphalerite quaternary chalcogenides to that of zinc-blende binaries in order to fully understand the origin of the low thermal conductivity these quaternary chalcogenides possess.

Introduction

Chalcogenides continue to be of interest for a variety of applications due to the unique physical properties that are directly related to specific bonding schemes and attributes, including optoelectronics and photovoltaics,[1–7] topological insulators,[8,9] thermoelectrics,[10,11] superconductivity[12–14] and magneto-ferroics.[15,16] New chalcogenide compositions expand our library of materials, and provide potential new discoveries through modification of the physical properties, transport mechanisms and processing conditions. Quaternary chalcogenides have recently been intensely investigated due to their promising potential for energy conversion applications. Many compositions have been explored taking into consideration environmental implications, while atypical transport properties for certain materials have also been reported.[17–24] Some quaternary chalcogenides are known copper rich compositions,[25–28] while others are derivatives of II-VI binaries that can be thought of as being formed by specific cation sublattice substitution.[29–31] For this latter case, compositions with the well-known kesterite crystal structure (I_2-II-IV-VI_4, where I=Cu or Ag, II=Zn or Cd, IV=Si, Ge or Sn, and VI=S, Se or Te) are an example.[32] Another family of quaternary

chalcogenides, I-II_2-III-VI_4 with III=Ga or In, can be understood as derivatives from the II-VI binary zinc-blende structure by cation substitutions, with four Zn^{2+} replaced by three cations $I^{1+}(II^{2+})_2III^{3+}$ such that the overall valence and charge neutrality is preserved from that of the "parent" II-VI composition.[32] These materials are semiconductors, the selenides and tellurides having 1 to 1.5 eV bandgaps that can be tuned via doping to optimize their desired properties.[33–36] Thus far only selenide and telluride compositions have been investigated. Herein we report the synthesis and temperature-dependent structural, thermal and electrical properties of $Cu_{1+x}Zn_{2-x}InS_4$, with x = 0, 0.15, and 0.3. The approach to doping via variation in composition resulted in dramatic changes in the electronic transport. Furthermore, the temperature-dependent structural and thermal properties of $CuZn_2InSe_4$ were also investigated in this study and the Grüneisen parameters for both $CuZn_2InS_4$ and $CuZn_2InSe_4$ were evaluated in order to quantify the anharmonicity in these materials. Our findings are compared with thermal properties of zinc-blende binaries in order to undertake a more comprehensive investigation of the structure-property relationships of these materials and present a study that contributes to the fundamental understanding of the physical properties of these quaternary chalcogenides.

a. Department of Physics, University of South Florida, Tampa, FL, 33620, USA.
b. Faculty of Chemistry and Food Chemistry, Technische Universität Dresden, 01062 Dresden, Germany.
c. Materials Science and Technology Division, Oak Ridge National Laboratory, Oak Ridge, TN 37831, USA.
d. Material Measurement Laboratory, National Institute of Standards and Technology Gaithersburg, MD 20899, USA.
e. Department of Materials Science and Engineering, University of Maryland, College Park, MD 20742, USA.
* Corresponding author: gnolas@usf.edu

Experimental

The quaternary chalcogenides $Cu_{1+x}Zn_{2-x}InS_4$ (x = 0, 0.15, and 0.3) were prepared by direct reaction of commercially available high purity elements. Copper powder (99.9 %, Alfa Aesar), Zn powder (99.9999 %, Alfa Aesar), In shot (99.99 %, Alfa Aesar) and S pieces (99.999 %, Alfa Aesar) were loaded into silica ampoules in the nominal compositions $CuZn_2InS_4$, $Cu_{1.15}Zn_{1.85}InS_4$ and $Cu_{1.3}Zn_{1.7}InS_4$.[37] Each reaction ampoule was

inserted in a quartz tube and evacuated before sealing. $CuZn_2InS_4$ was reacted at 973 K for 4 days while the off-stochiometric compositions were reacted at 1073 K for 4 days, all with a heating rate of 20 K/h. The furnaces were subsequently turned off allowing the specimens to cool down to room temperature. The specimens were then ground, cold pressed into pellets and sealed in a quartz tube under vacuum for annealing at 873 K for 7 days. Densification of the finely ground and sieved (325 mesh; 45 μm) specimens was accomplished by spark plasma sintering (SPS, Thermal Technology model #10-3). Each specimen was loaded into a custom-designed WC punch-die assembly and densified at 400 MPa and 723 K. The temperature ramp rate was 25 K/min. The pressure and current were maintained for 30 minutes once this temperature was reached resulting in dense polycrystalline materials > 95 % of theoretical density for all specimens.

Crystal structure analyses of $Cu_{1+x}Zn_{2-x}InS_4$ (x = 0, 0.15, and 0.3) were done by Rietveld structure refinement of X-ray diffraction (XRD) measurements and the stoichiometries were corroborated by energy dispersive spectroscopy (EDS). Powder XRD data were collected with a Bruker-AXS D8 Focus diffractometer in Bragg-Brentano geometry with Cu K_α radiation and a graphite monochromator. Rietveld refinement was performed using GSAS II software.[38] The initial parameters for structure refinement were based on structural data previously reported for selenide and telluride materials.[33,35] EDS of the sintered specimens were performed using an Oxford INCA X-Sight 7852M equipped scanning electron microscope (SEM JEOL JSM-6390LV). Before SPS densification, differential thermal analysis (DTA) and thermogravimetric analysis (TGA) under nitrogen gas flow were performed using a TA Instruments Q600 apparatus and showed that these sphalerite quaternary chalcogenides are stable up to 823 K. Temperature dependent electrical resistivity, ρ, and Seebeck coefficient, S, were measured on parallelepipeds (2 mm x 2 mm x 10 mm) using a ULVAC ZEM-3 system. The experimental uncertainty was estimated to be ± 5% and ± 8% for ρ and S, respectively. All stated uncertainties are 1 standard deviation (no expansion). Thermal diffusivity, α, was measured employing the laser flash diffusivity method (NETZSCH LFA457 system) under Ar flow. The experimental uncertainty in α measurements were estimated to be ± 5%. Temperature dependent thermal conductivity, κ, was calculated using the equation $\kappa = D\alpha C_p$, where D and C_p are the measured density from geometry and specific heat capacity, respectively. Specific heat capacity C_p ($\approx C_v$) was estimated from the Dulong-Petit limit [39], $C_v = 3nR$, where n and R are the number of atoms per formula unit and the ideal gas constant, respectively. At high temperature this may sometimes result in an underestimation of C_p, thus affecting κ, however for $CuZn_2InS_4$ we estimate C_p–C_v to be less than 1% at room temperature and smaller at lower temperatures. Room temperature four-probe Hall measurements (0.5 mm x 2 mm x 5 mm) were collected in magnetic fields up to 1.2 T. Alternating the polarity of the field eliminated voltage probe misalignment effects. Isobaric heat capacity, Cp, measurements from 300 K to 2 K were performed using a commercial Quantum Design

Physical Property Measurement System using thermal N-grease and appropriate addenda. The uncertainty across the entire measured temperature range was within ±5%.

The low temperature XRD data was obtained using a specialized Empyrean powder X-ray diffractometer (parallel beam, hybrid 220-Ge Monochromator, Cu-Kα_1 radiation) and Pixcel3D detector with a customized sample holder in an ARS DE-102 closed-cycle helium cryostat with beryllium windows, assuring isothermal conditions in the temperature range of 50 K to 300(1) K. The powder specimens were prepared between amorphous tapes and fixed in the measurement position. The XRD patterns were measured in transmission geometry in the 2θ range of 10° to 90°. Rietveld refinement was carried out using TOPAS Academic (version 5)[40] with peak profiles modeled with the fundamental parameter approach implemented in TOPAS. The geometry employed can produce a systematic deviation as compared to our room temperature measurements. The instrumental resolution function was therefore determined using NIST SRM 640d silicon powder as a standard to reduce such effects.

Results and Discussion

Figure 1 shows the room temperature experimentally observed, calculated and difference patterns from our Rietveld refinement results of the three compositions investigated for this study. $CuZn_2InS_4$ was phase-pure while trace amounts of CuS was refined to be ≈ 2 % for $Cu_{1.15}Zn_{1.85}InS_4$ and $Cu_{1.3}Zn_{1.7}InS_4$. Our refinement results indicated compositions very close to that of the nominal compositions. The small broadening in the XRD peaks is due to disorder on the cation sublattice. These quaternary chalcogenides compounds crystallize in the sphalerite structure with space group $F\bar{4}3m$. There are two crystallographic sites, with the metal cations (Cu, Zn, In) and S occupying the $4a$ (0, 0, 0) and $4c$ (¼, ¼, ¼) crystallographic sites, respectively. Each S atom is surrounded by four cation atoms in a tetrahedral geometry, as shown in Figure 2. Cation-S bond distances are 2.3920(6) Å, 2.3788(4) Å and 2.3788(4) Å, for $CuZn_2InS_4$, $Cu_{1.15}Zn_{1.85}InS_4$ and $Cu_{1.3}Zn_{1.7}InS_4$, respectively. The decrease in bond distance and lattice constant are directly associated with the different ionic radii of Cu and Zn. The results of our structure refinements are summarized in Table 1.

Temperature dependent S and ρ data are shown in Figures 3(a) and (b), respectively. The high electrical resistance of $CuZn_2InS_4$ prevented ρ and S measurements for this composition. The ρ and S values decrease with increasing (decreasing) Cu (Zn) content for the off-stoichiometric compositions. The decrease in ρ with stoichiometric variation, shown in Figure 3(a), is directly related to the increase in carrier concentration with increasing Cu content (*i.e.*, increasing ratio of Cu-to-Zn content). Our Hall measurements indicated room temperature hole concentrations, p, of 1.5 x 10^{18}/cm³ and 2.0 x 10^{20}/cm³ for $Cu_{1.15}ZnInS_4$ and $Cu_{1.3}ZnInS_4$, respectively. This relatively low doping efficiency, estimated to be approximately 25% assuming

one carrier per excess Cu, is typical for such inorganic materials. As shown in the inset in Figure 3(a), a fit of the form $\rho = \rho_o e^{E_a/k_BT}$, where E_a is the activation energy and k_B is the Boltzmann constant, result in E_a = 0.24 and 0.10 eV for $Cu_{1.15}Zn_{1.85}InS_4$ and $Cu_{1.3}Zn_{1.7}InS_4$, respectively, and indicates a shift of the Fermi level towards the valence band with increasing Cu content. The effective mass, m^*, may be estimated assuming a single parabolic band model, where
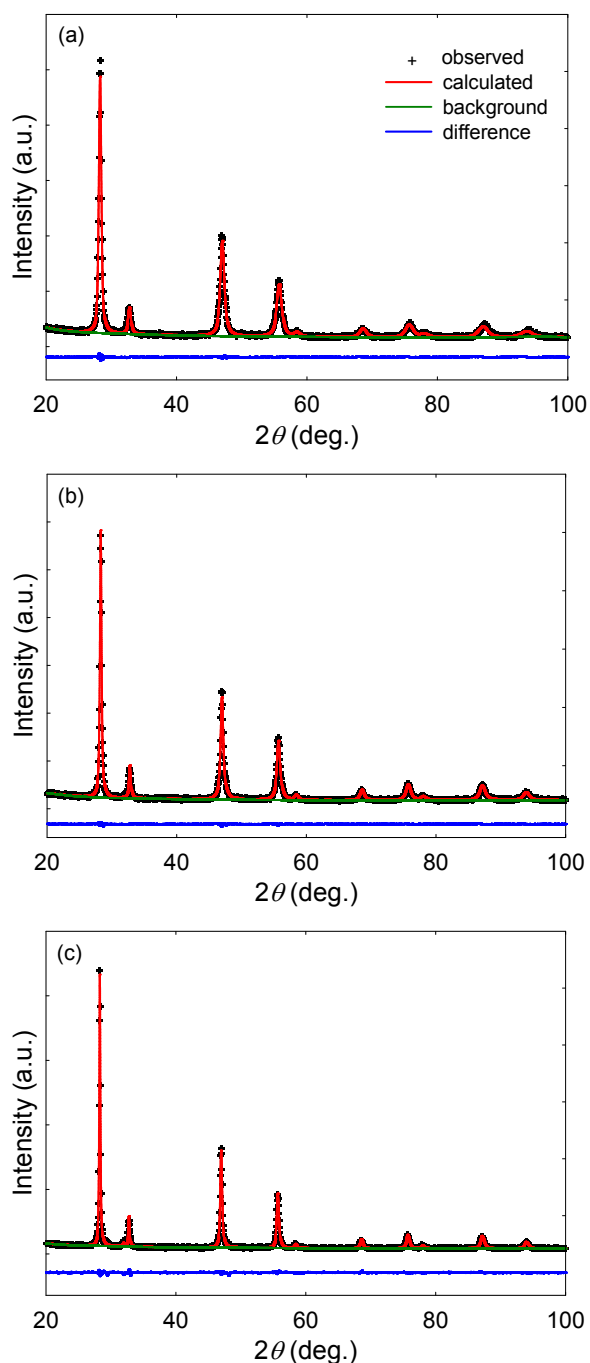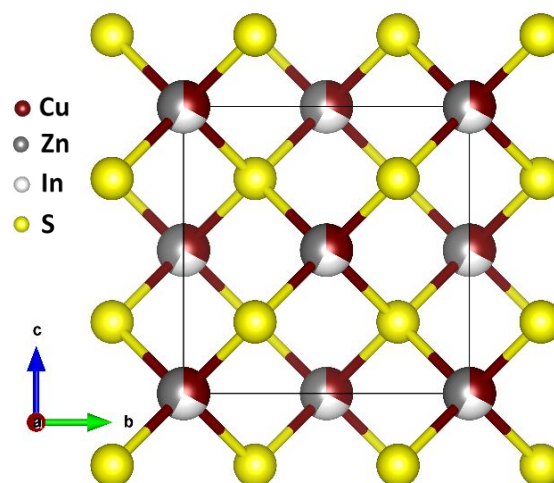

Figure 2. The crystal structure of sphalerite $CuZnInS_4$ illustrating the cation atoms (Cu/Zn/In) and the S atoms occupying the $4a$ (0, 0, 0) and $4c$ (¼, ¼, ¼) Wyckoff positions, respectively.

$$S = \frac{k_B}{e}\left(\frac{(2+r)F_{r+1}(\eta)}{(1+r)F_r(\eta)} - \eta\right), \tag{1}$$

$$p = \frac{4\pi(2m^*k_BT)^{3/2}}{h^3}F_{1/2}(\eta) \tag{2}$$

and

$$F_r(\eta) = \int_0^\infty \frac{E^{*r}}{e^{(E^*-\eta)}+1}dE^*. \tag{3}$$

Here E^* (=E/k_BT) is the reduced energy, η (=E_F/k_BT) is the reduced Fermi energy, F_r is the Fermi integral of order r, h is the Planck constant and r is the scattering parameter with values of r = 0 for acoustic phonon scattering and r = 2 for ionized impurity scattering. The intermediate value of r = 1 was used for estimations of m^*. Utilizing the room temperatures p values from our Hall measurements, m^* values (0.1 m_e) for $Cu_{1.15}Zn_{1.85}InS_4$ and $Cu_{1.3}Zn_{1.7}InS_4$ are over an order of magnitude smaller than that reported for tellurium-based sphalerite quaternary chalcogenides,[33–35] indicating relatively steep curvature of the valence band for the sulfur-based materials. In addition, these compositions have relatively low room temperature Hall mobilities, μ, of 1.5 $cm^2V^{-1}s^{-1}$ and 0.1 $cm^2V^{-1}s^{-1}$ for $Cu_{1.15}Zn_{1.85}InS_4$ and $Cu_{1.3}Zn_{1.7}InS_4$, respectively. These μ values are smaller compared to that of $CuZn_2InTe_4$ and $CuCd_2InTe$,[33] and may indicate shorter carrier relaxation times as compared to the telluride compositions. In addition, our lower temperature p and S data suggests a second band, with lower activation energy, may be involved in the electrical transport. Theoretical investigations of the band structure would be useful in elucidating further specifics of these findings.

Figure 1. XRD data for (a) $CuZn_2InS_4$, (b) $Cu_{1.15}Zn_{1.85}InS_4$ and (c) $Cu_{1.3}Zn_{1.7}InS_4$, including the profile fit and profile difference from Rietveld refinement.

Figure 4 shows the temperature dependent κ data for the three specimens prepared for this investigation. An excess of Cu

Table 1: Rietveld refinement results for $Cu_{1+x}Zn_{2-x}InS_4$ (x = 0, 0.15, and 0.30).

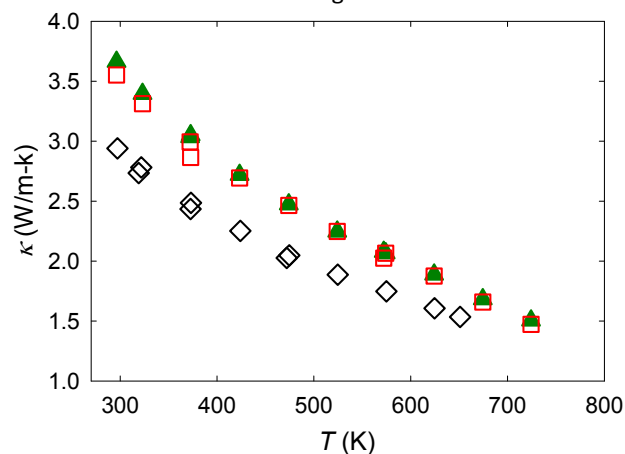| Nominal composition	$CuZn_2InS_4$	$Cu_{1.15}Zn_{1.85}InS_4$	$Cu_{1.3}Zn_{1.7}InS_4$
Refined composition	$CuZn_2InS_4$	$Cu_{1.15}Zn_{1.85}InS_4$	$Cu_{1.3}Zn_{1.7}InS_4$
Space group, Z	$F\overline{4}3m$ (#216), 1		
Lattice constant (Å)	5.5240 (12)	5.4937 (8)	5.4912 (4)
V (Å^3)	168.56(11)	165.80 (7)	165.58 (4)
D_{cal} (g/cm^3)	4.3086	4.3775	4.3807
Radiation	Graphite monochromated Cu Kα (1.54056 Å)		
2Θ range (deg.)	20-100		
Step width (deg.)	0.02		
wR_p, R_p	0.06322, 0.05053	0.05975, 0.04615	0.04996, 0.03726
Reduced χ^2	1.548	1.450	1.336
U_{iso} (Å^2) for Cu/Zn/In	0.0244	0.0247	0.0211
U_{iso} (Å^2) for S	0.0142	0.0236	0.0174

Atomic positions: Cu/Zn/In, 4a (0, 0, 0); S, 4c (¼, ¼, ¼)
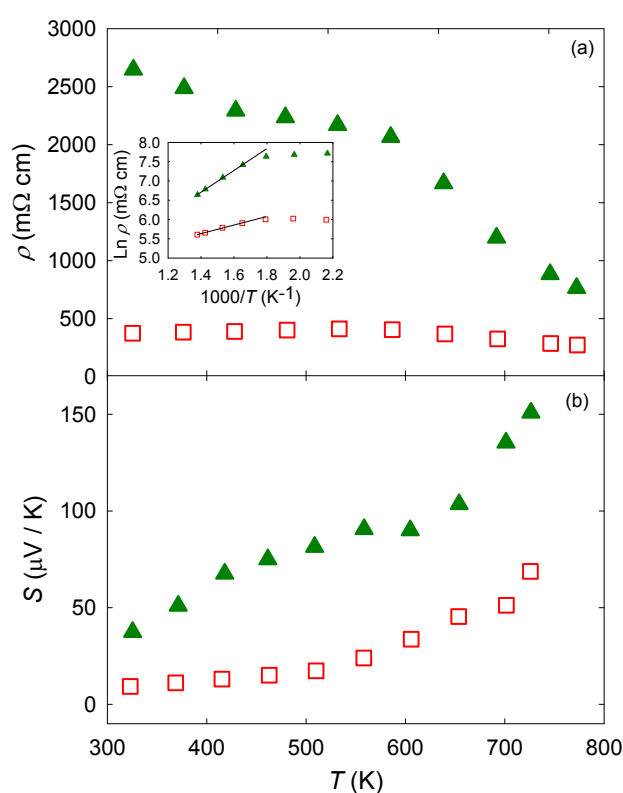
Figure 3. Temperature-dependent (a) ρ and (b) S for $Cu_{1.15}Zn_{1.85}InS_4$ (▲) and $Cu_{1.3}Zn_{1.7}InS_4$ (□). The inset shows Ln ρ versus 1000/T data where the solid line is a fit of the form $\rho = \rho_o e^{E_a/k_B T}$.

Figure 4. Temperature-dependent κ for $CuZn_2InS_4$ (◇), $Cu1_{.15}Zn_{1.85}InS_4$ (▲) and $Cu_{1.3}Zn_{1.7}InS_4$ (□).

resulted in a small increase in κ, partly due to an increase in the electronic contribution to κ, implying that low κ values are intrinsic to these materials. Figure 5 shows the C_p versus T data for $CuZn_2InS_4$. The C_p data approaches the Dulong-Petit limit near room temperature, an indication that the optic and acoustic mode frequencies are fully excited at 300 K. The inset shows C_p/T versus T^2 data with a straight line fit of the form $C_p = \alpha T + \beta T^3$, where α is the Sommerfeld coefficient of the electronic contribution to C_p and β is the lattice contribution. A Debye temperature, θ_D, of 296 K was obtained employing $\theta_D = (12\pi^4 Rn/5\beta)^{1/3}$, [41] where R is the molar gas constant, n is the

number atoms per formula unit and $\beta = 0.6$ mJ mol^{-1}K^{-4} obtained from the fit shown in Figure 5. The null α value (0.05 mJ mol^{-1}K^{-2}) indicates a very small density of states at the Fermi level, consistent with the very high resistance for this material. Figure 6 shows the lattice parameter, a_o, as a function of temperature for $CuZn_2InS_4$. The temperature dependent XRD data are summarized in Table 2. As shown in the Figure, a_o increases with temperature. A least square fit to a second order polynomial $a_o = a_0 + a_1 T + a_2 T^2$ was used to model the temperature dependence of a_o, where the a_o fit values are listed in Table 3. The linear thermal expansion, CTE, was calculated to be 8.7 x 10^{-6} K^{-1} at 300 K using the measured lattice parameters over the entire temperature region, with CTE = 1/a_o (δa_o/δT)$_P$. The Grüneisen parameter, γ, can then be estimated from the relation $\gamma = \alpha_V BV/C_V$, where α_V is volume thermal expansion coefficient (α_V = 3CTE for cubic materials), B is the bulk modulus, V is the unit cell volume and C_V is the isochoric heat capacity. Using the room temperature value of B for ZnS[42] we estimate γ = 1, in reasonable agreement with the calculated value by Shi et al. for sphalerite $CuZn_2InTe_4$[43]. In order to extend our investigation of these sphalerite quaternary chalcogenides, and more completely investigate the structure-property relationships and low κ in these materials we also measured and analyzed the temperature dependent structural data and

ARTICLE

*C*p of $CuZn_2InSe_4$ in a similar manner as described above for $CuZn_2InS_4$. The *C*p data is shown in Figure 7, with the inset showing a_o as a function of temperature from our temperature
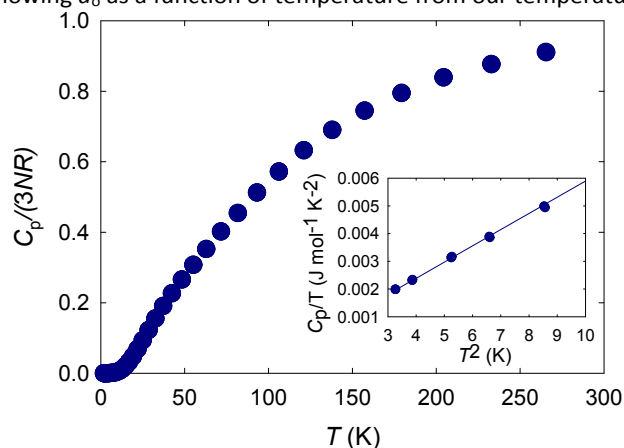

Figure 5. Temperature-dependent C_p data for $CuZn_2InS_4$ with the inset showing C_p/T versus T^2 data at low temperatures and the solid line is a fit of the form $C_p/T = \alpha + \beta T^2$.
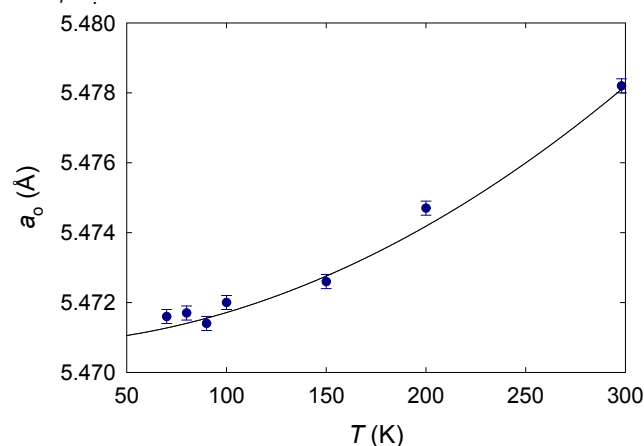

Figure 6. Temperature-dependent lattice parameter for $CuZn_2InS_4$.

Table 2. Rietveld Refinement Results for $CuZn_2InS_4$.

T (K)	298 K	200 K	150 K	100 K	90 K	80 K	70 K	60 K	50 K
a (Å)	5.4782(2)	5.4747(2)	5.4726(2)	5.472(2)	5.4714(2)	5.4717(2)	5.4716(2)	5.4704(2)	5.4701(2)
V (Å³)	164.407(19)	164.094(19)	163.900(19)	163.849(19)	163.792(19)	163.82(2)	163.81(2)	163.70(2)	163.68(2)
U_{iso} (Å²) for Cu/Zn/In	0.046(2)	0.0400(6)	0.0372(6)	0.0367(6)	0.0361(6)	0.0347(6)	0.0343(6)	0.0358(6)	0.0343(6)
U_{iso} (Å²) for S	0.047(3)	0.0432(13)	0.0441(13)	0.0366(12)	0.0401(13)	0.0417(13)	0.0385(13)	0.0389(13)	0.0389(13)
R_{Bragg}	4.72	4.08	3.66	3.8	3.63	4.3	3.67	3.71	3.69
GOF	1.264	1.28	1.299	1.323	1.298	1.326	1.326	1.329	1.337

Atomic positions: Cu/Zn/In, 4*a* (0, 0, 0); S, 4*c* (¼, ¼, ¼)

dependent XRD data for $CuZn_2InSe_4$ summarized in Table 4. From our analyses $\beta = 0.9 \text{ mJ mol}^{-1}\text{K}^{-4}$ and θ_D = 259 K for $CuZn_2InSe_4$. The heavier chalcogen (Se) in the sphalerite structure results in a decrease in θ_D. The CTE of $CuZn_2InSe_4$ at 300 K is 9.0 x 10^{-6} K⁻¹ resulting in γ = 1, and suggests that the crystal lattices of $CuZn_2InS_4$ and $CuZn_2InSe_4$ display similar anharmonicity at high temperatures.

Over four decades ago Slack showed that the lattice contribution to κ is $BMV^{1/3}\theta_D^3 n^{-2/3}T^{-1}\gamma^{-2}$ for materials with similar crystal structures, where B is a constant, M is the average mass of an atom in a crystal, V is the unit cell volume, n is the number of atoms per primitive cell and T is the absolute temperature.[44] Figure 8 shows room temperature κ versus $MV^{1/3}\theta_D^3$ for zinc-blende binary semiconductors,[42] as well as for $CuZn_2InS_4$ and $CuZn_2InSe_4$. We include $CuZn_2InTe_4$ for completeness of this comparison.[34, 43] As shown in the figure, the quaternary chalcogenides clearly have lower κ values. Although γ for the sphalerite quaternary chalcogenides is somewhat larger in comparison to the binary zinc-blende compositions, the much lower κ values for the quaternary chalcogenides must be related to their similar phonon scattering mechanisms. First principles simulations on

$CuZn_2InTe_4$ revealed a suppression of acoustic modes by low frequency optical phonons leading to enhanced phonon scattering.[43] A similar phonon-scattering mechanism is presumably the case for all sphalerite quaternary chalcogenides (*i.e.*, S, Se and Te-based), and together with a larger γ results in the lower κ values for these materials.

Table 3. Parameters for the polynomial function $a_o = a_0 + a_1T + a_2T^2$ from the temperature dependent lattice parameter data fit.

	a_0 (Å)	a_1 (10^{-5} Å/K)	a_2 (10^{-8} Å/K²)
$CuZn_2InS_4$	5.47	0.165	7.68
$CuZn_2InSe_4$	5.72	2.39	4.67

Conclusions

Polycrystalline quaternary chalcogenides $Cu_{1+x}Zn_{2-x}InS_4$ (x = 0,

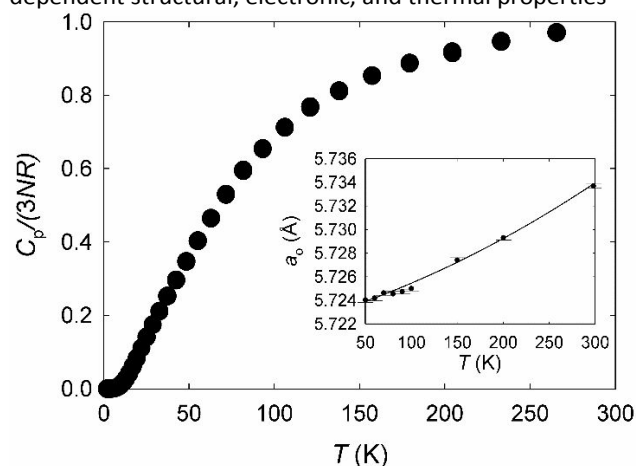0.15, and 0.3) were synthesized and their temperature dependent structural, electronic, and thermal properties

Figure 7. Temperature-dependent C_p for CuZn$_2$InSe$_4$ with data approaching the Dulong-

Petit limit near room temperature. The inset shows temperature dependent a_0 for CuZn$_2$InSe$_4$ together with a fit of the form $a_o = a_0 + a_1 T + a_2 T^2$.

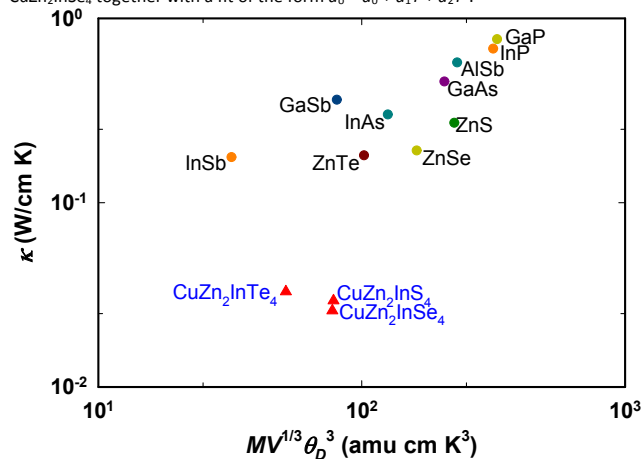Figure 8. Room temperature κ versus $MV^{1/3}\theta_D^3$ for III-V and II-VI binaries, CuZn$_2$InS$_4$, CuZn$_2$InSe$_4$ and CuZn$_2$InTe$_4$.

Table 4. Rietveld Refinement Results for CuZn$_2$InSe$_4$.

T (K)	298 K	200 K	150 K	100 K	90 K	80 K	70 K	60 K	50 K
a (Å)	5.7337(3)	5.72930(4)	5.72741(4)	5.72499(4)	5.72473(4)	5.72455(4)	5.72462(4)	5.72418(4)	5.72403(4)
V (Å³)	188.50(3)	188.064(4)	187.877(4)	187.640(4)	187.614(4)	187.596(4)	187.603(4)	187.560(4)	187.545(4)
U$_{iso}$ (Å²) for Cu/Zn/In	0.039(3)	0.0337(10)	0.0294(9)	0.0305(8)	0.0263(10)	0.0287(9)	0.0298(9)	0.0303(10)	0.0305(9)
U$_{iso}$ (Å²) for Se	0.025(3)	0.0228(8)	0.0166(7)	0.0154(6)	0.0168(8)	0.0160(6)	0.0189(7)	0.0213(8)	0.0173(6)
R$_{Bragg}$	4.52	5.53	5.97	4.1	4.66	4.83	4.63	5	5.99
GOF	1.291	1.314	1.327	1.329	1.34	1.338	1.321	1.347	1.353

Atomic positions: Cu/Zn/In, 4a (0, 0, 0); Se, 4c (¼, ¼, ¼)

investigated. A transition from insulating to semiconducting behavior was revealed with excess Cu, and the intrinsically low thermal conductivity did not change substantially with carrier concentration. Temperature-dependent structural and thermal properties were investigated for CuZn$_2$InS$_4$ as well as CuZn$_2$InSe$_4$ in order to investigate and compare the anharmonicity of the sphalerites with that of the "parent" zinc-blende binaries. Similar lattice anharmonicity, together with a comparable average atomic mass and unit cell volume for the sphalerite quaternary chalcogenides, suggest similar phonon-scattering mechanisms occurring for CuZn$_2$InS$_4$ and CuZn$_2$InSe$_4$ as that for CuZn$_2$InTe$_4$ resulting in much lower κ for these quaternary chalcogenides as compared to the "parent" binary compositions.

Conflicts of interest

There are no conflicts to declare.

Notes and references

1   A. Swarnkar, W. J. Mir, R. Chakraborty, M. Jagadeeswararao, T. Sheikh and A. Nag, *Chem. Mater.*, 2019, **31**, 565–575.
2   A. A. Rockett, *Curr. Opin. Solid State Mater. Sci.*, 2010, **14**, 143–148.
3   D. Fuertes Marrón, E. Cánovas, M. Y. Levy, A. Martí, A. Luque, M. Afshar, J. Albert, S. Lehmann, D. Abou-Ras, S. Sadewasser and N. Barreau, *Sol. Energy Mater. Sol. Cells*, 2010, **94**, 1912–1918.
4   Q. Cao, O. Gunawan, M. Copel, K. B. Reuter, S. J. Chey, V. R. Deline and D. B. Mitzi, *Adv. Energy Mater.*, 2011, **1**, 845–853.

5 T. Todorov and D. B. Mitzi, *Eur. J. Inorg. Chem.*, 2010, 2010, 17–28.

6 S. Fiechter, Y. Tomm, M. Kanis, R. Scheer and W. Kautek, *Phys. status solidi*, 2008, **245**, 1761–1771.

7 D. Kerroum, H. Bouafia, B. Sahli, S. Hiadsi, B. Abidri, A. Bouaza and M. A. Timaoui, *Optik*, 2017, **139**, 315–327.

8 W. Feng, D. Xiao, J. Ding and Y. Yao, *Phys. Rev. Lett.*, 2011, **106**, 016402.

9 S. Chen, X. G. Gong, C. G. Duan, Z. Q. Zhu, J. H. Chu, A. Walsh, Y. G. Yao, J. Ma and S. H. Wei, *Phys. Rev. B*, 2011, **83**, 245202.

10 Y. Shi, C. Sturm and H. Kleinke, *J. Solid State Chem.*, 2019, **270**, 273–279.

11 W. Shi, A. R. Khabibullin, D. Hobbis, G. S. Nolas and L. M. Woods, *J. Appl. Phys.*, 2019, **125**, 155101.

12 D. V Denisov and K. D. Tsendin, *J. Optoelectron. Adv. Mater.*, 2003, **5**, 1011–1016.

13 K. Deguchi, Y. Takano and Y. Mizuguchi, *Sci. Technol. Adv. Mater.*, 2012, **13**, 054303.

14 Y. Mizuguchi and Y. Takano, *J. Phys. Soc. Japan*, 2010, **79**, 102001.

15 G. Nénert and T. T. M. Palstra, *J. Phys. Condens. Matter*, 2009, **21**, 176002.

16 T. Fries, Y. Shapira, F. Palacio and M. C. Morón, *Phys. Rev. B - Condens. Matter Mater. Phys.*, 1997, **56**, 5424–5431.

17 P. Kush and S. Deka, *ChemNanoMat*, 2019, **5**, 373–402.

18 D. S. Dhawale, A. Ali and A. C. Lokhande, *Sustain. Energy Fuels*, 2019, **3**, 1365–1383.

19 K. Wei, L. Beauchemin, H. Wang, W. D. Porter, J. Martin and G. S. Nolas, *J. Alloys Compd.*, 2015, **650**, 844–847.

20 Y. Dong, H. Wang and G. S. Nolas, *Phys. status solidi - Rapid Res. Lett.*, 2014, **8**, 61–64.

21 Y. Dong, H. Wang and G. S. Nolas, *Inorg. Chem.*, 2013, **52**, 14364–14367.

22 K. Wei, A. R. Khabibullin, T. Stedman, L. M. Woods and G. S. Nolas, *J. Appl. Phys.*, 2017, **122**, 105109.

23 K. Wei and G. S. Nolas, *J. Solid State Chem.*, 2015, **226**, 215–218.

24 Y. Dong, B. Eckert, H. Wang, X. Zeng, T. M. Tritt and G. S. Nolas, *Dalt. Trans.*, 2015, **44**, 9014–9019.

25 V. Pavan Kumar, G. Guélou, P. Lemoine, B. Raveau, A. R. Supka, R. Al Rahal Al Orabi, M. Fornari, K. Suekuni and E. Guilmeau, *Angew. Chemie*, 2019, **131**, 15601–15609.

26 Y. Bouyrie, V. Ohorodniichuk, S. Sassi, P. Masschelein, A. Dauscher, C. Candolfi and B. Lenoir, *J. Electron. Mater.*, 2017, **46**, 2684–2690.

27 X. Lu, D. T. Morelli, Y. Xia, F. Zhou, V. Ozolins, H. Chi, X. Zhou and C. Uher, *Adv. Energy Mater.*, 2013, **3**, 342–348.

28 T. Barbier, S. Rollin-Martinet, P. Lemoine, F. Gascoin, A. Kaltzoglou, P. Vaqueiro, A. V. Powell and E. Guilmeau, *J. Am. Ceram. Soc.*, 2016, **99**, 51–56.

29 S. Chen, X. G. Gong, A. Walsh and S. H. Wei, *Phys. Rev. B - Condens. Matter Mater. Phys.*, 2009, **79**, 165211.

30 Y. Dong, A. R. Khabibullin, K. Wei, Z.-H. Ge, J. Martin, J. R. Salvador, L. M. Woods and G. S. Nolas, *Appl. Phys. Lett.*, 2014, **104**, 252107.

31 S. Chen, A. Walsh, Y. Luo, J. H. Yang, X. G. Gong and S. H. Wei, *Phys. Rev. B - Condens. Matter Mater. Phys.*, 2010, **82**, 195203.

32 B. R. Pamplin, *J. Phys. Chem. Solids*, 1964, **25**, 675–684.

33 G. S. Nolas, M. S. Hassan, Y. Dong and J. Martin, *J. Solid State Chem.*, 2016, **242**, 50–54.

34 D. Hobbis, K. Wei, H. Wang and G. S. Nolas, *J. Alloys Compd.*, 2018, **743**, 543–546.

35 D. Hobbis, W. Shi, A. Popescu, K. Wei, R. E. Baumbach, H. Wang, L. M. Woods and G. S. Nolas, *Dalt. Trans.*, 2020, **49**, 2273–2279.

36 G. S. Nolas, H. Poddig, W. Shi, L. M. Woods, J. Martin and H. Wang, *J. Solid State Chem.*, 2021, **297**, 122058.

37 Certain commercial equipment, instruments, software, or materials are identified in this document. Such identification does not imply recommendation or endorsement by the National Institute of Standards and Technology, nor does it imply that the materials or equipment identified are necessarily the best available for the purpose.

38 B. H. Toby and R. B. Von Dreele, *J. Appl. Crystallogr.*, 2013, **46**, 544–549.

39 H. Wang, W. D. Porter, H. Böttner, J. König, L. Chen, S. Bai, T. M. Tritt, A. Mayolet, J. Senawiratne, C. Smith, F. Harris, P. Gilbert, J. Sharp, J. Lo, H. Kleinke and L. Kiss, *J. Electron. Mater.*, 2013, **42**, 1073–1084.

40 A. A. Coelho, *J. Appl. Crystallogr.*, 2018, **51**, 210–218.

41 C. Kittel, *Introduction to solid state physics*, John Wiley & Sons, Inc., New York, 2005.

42 S. Adachi, *Properties of Group-IV, III-V II-VI Semiconductors*, John Wiley & Sons, Ltd, West Sussex, 2005.

43 W. Shi, T. Pandey, L. Lindsay and L. M. Woods, *Phys. Rev. Mater.*, 2021, **5**, 045401.

44 G. A. Slack, *Solid State Phys. - Adv. Res. Appl.*, 1979, **34**, 1–71.